Ferroelectric manipulation and enhancement of Rashba spin splitting in van der Waals heterostructures

Zhaofeng Liang,[1,2,3] Jinsen Zhang,[4] Chenqiang Hua,[5,*] Yao Wang,[4] and Fei Song[1,2,3,†]

[1]*Shanghai Institute of Applied Physics, Chinese Academy of Sciences, Shanghai 201204, People's Republic of China*

[2]*Shanghai Synchrotron Radiation Facility, Shanghai Advanced Research Institute, Chinese Academy of Sciences, Shanghai 201204, People's Republic of China*

[3]*University of Chinese Academy of Sciences, Beijing 101000, People's Republic of China*

[4]*College of Materials Science and Engineering, Zhejiang University of Technology, Hangzhou 310014, People's Republic of China*

[5]*Hangzhou International Innovation Institute, Beihang University, Yuhang District, Hangzhou 311115, People's Republic of China*

(Received 9 April 2024; revised 4 July 2024; accepted 19 July 2024; published 5 August 2024)

Ferroelectric (FE) Rashba semiconductors, a class of multifunctional materials with potential applications in spintronic devices, have attracted increasing interests recently. Herein, we employ first-principles calculations and the **k**·**p** Hamiltonian method to comprehensively investigate the Rashba effect in MX/α-In_2Se_3 (MX=GaTe and InSe) van der Waals (vdW) heterobilayers and reveal the mechanism underlying the FE manipulation of Rashba spin splitting. Remarkably, the strength of spin splitting in the GaTe/α-In_2Se_3 heterobilayer has been significantly enhanced several times with respect to the intrinsic α-In_2Se_3 monolayer. This enhancement is attributed to the effective interfacial electric field contributed from the strong interfacial charge transfer and mirror symmetry breaking. Furthermore, the symmetric and asymmetric α-In_2Se_3/GaTe/α-In_2Se_3 sandwiched structures with four switchable states verify that Rashba spin splitting can be effectively tuned by the FE switch, and its enhancement is achievable if the mirror symmetry is not preserved. Interestingly, spin Hall conductivity can also be manipulated by the spin-orbit coupling associated with the intensified interfacial charge transfer. Our findings highlight the appealing potential of vdW heterostructures as an ideal platform for expanding the family of FE Rashba semiconductors and further promoting their applications in spintronics.

DOI: 10.1103/PhysRevB.110.085110

I. INTRODUCTION

Spin-orbit coupling (SOC) not only plays a crucial role in numerous physical phenomena such as the spin Hall effect (SHE) [1] and the quantum Hall states [2] but also in realizing the electric control of spin degree freedom in spintronic devices made of nonmagnetic materials [3,4]. When crystals are inversion asymmetric with a nonzero gradient of electrostatic potential, the so-called Rashba effect [5] appears due to the effective SOC, which can be characterized as the splitting of spin-degenerate parabolic bands into two subbands with opposite spins and energy-momentum dispersions:

$$E_{\pm}(k) = \frac{\hbar^2 k^2}{2m^*} \pm \alpha_R k, \tag{1}$$

where k is the in-plane momentum, m^* is the effective mass of electron, and α_R represents the strength of the Rashba effect. Owing to such a spin-momentum locking mechanism, Rashba SOC can be used for efficient spin-to-charge conversion and nonlinear transport effect, which are appealing for applications of spintronic devices [4,6–8]. Intriguingly, with recently discovered materials that have been synthesized, the Rashba effect has also led to various exotic properties and discoveries in physics [9], such as synergetic effects between Rashba valleys and quantum Hall states [2], topological superconductivity [10], and the topological Rashba-like surface state [11].

On the other hand, ferroelectricity (FE), manifested by spontaneous and switchable polarization, also originates from the broken centrosymmetry of crystals. From this perspective, it is natural to propose that both the Rashba effect and FE can coexist in a single-phase material, where the spin texture can be reversed by switching polarization via an extensive electric field [12]. In fact, the Rashba splitting and FE in three-dimensional (3D) GeTe was predicted theoretically and subsequently confirmed by experiments [13–16]. More examples can also be found in BiTeI [17,18], hexagonal semiconductors [19], and halide/oxide perovskites [20–22].

In contrast with the bulk systems, two-dimensional (2D) layered materials with the atomic thickness are more appealing for electronics and spintronics. To date, various 2D FE Rashba semiconductors, including layered $AgBiP_2X_6$ (X = S, Se, and Te) [23], tellurium thin film [24], group-IV and III-V binary monolayers [25], distorted 1T-phase transition-metal dichalcogenides (TMDs) monolayers [26], and sliding TMDs bilayers [27], have been predicted or experimentally proven case by case. Recently, an increasing number of potential FE Rashba materials has also been proposed using the high-throughput inverse design approach [28,29]. However, obvious spin splitting has rarely been observed experimentally due to the small SOC. Authors of prior studies have shown

*Contact author: huachenqiang@buaa.edu.cn
†Contact author: songfei@sinap.ac.cn

that 2D materials vertically stacked into van der Waals (vdW) heterostructures offer a unique advantage for engineering the band structure and deliberately manipulating giant SOC [30–33]. Therefore, instead of looking for intrinsic FE Rashba semiconductors, the more effective approach is to fabricate vdW heterostructures with strong interfacial interactions using out-of-plane polarized 2D FEs and other layered materials, which may achieve the control of FE and the enhancement of Rashba spin-splitting simultaneously.

In this paper, we systematically investigate the impact of the coupling effect between FE polarization and interfacial interaction on Rashba spin-splitting through first-principles calculations. Here, out-of-plane polarized α-In_2Se_3 [34,35] is adopted to fabricate the heterostructure with the group-III monochalcogenides monolayers. For comparison, GaTe and InSe are introduced as examples. Specifically, we find that the GaTe/α-In_2Se_3 heterobilayers are credited with the enhanced Rashba spin-splitting of conduction bands (CBs) around Γ due to the associative coupling between the interfacial and built-in electric field. Accordingly, the spin splitting can be effectively manipulated by switching the polarization direction of α-In_2Se_3. We also use the $\mathbf{k}\cdot\mathbf{p}$ Hamiltonian method to discuss the in-plane and out-of-plane spin polarization. Then the α-In_2Se_3/GaTe/α-In_2Se_3 sandwich heterostructure is also constructed. Bands become nearly degenerate in highly symmetric sandwich structures, while for all polarization up/down cases, obvious Rashba spin splitting emerges in the CBs, indicating the effect of polarization modulation. Finally, FE manipulations of spin-transport properties in the large Rashba SOC vdW systems have also been investigated.

II. COMPUTATIONAL DETAILS

First-principles calculations based on density functional theory (DFT) were performed in VASP [36]. The Perdew-Burke-Ernzerhof form within the generalized gradient approximation [37] and the projector augmented-wave pseudopotentials [38] were used to describe the electron exchange-correlation potential and core electrons, respectively. Here, Γ-centered k-point sampling was used for the Brillouin zone integration: $17 \times 17 \times 1$, while the kinetic energy cutoff for the plane-wave basis was set to 500 eV. During the geometry optimization, all atoms were fully relaxed with a force convergence criterion of 0.01 eV/Å by using the conjugated-gradient minimization scheme. The optimized lattice parameters of GaTe, InSe, and α-In_2Se_3 monolayers are 4.13, 4.09, and 4.10 Å, respectively, in good agreement with previous reports [39]. The 2D MX/α-In_2Se_3 heterobilayer was placed in the $x-y$ plane with a vacuum region thicker than 16 Å to avoid periodic interaction along the z axis. In addition, the DFT-D3 scheme with Becke-Jonson damping [40,41] was adopted to incorporate the dispersion coefficients, and the results of different vdW methods are summarized in the Supplemental Material (SM) [42] (see also Refs. [24,29,39–41,43–45] therein). For the electronic-structure calculations, SOC was considered to investigate the Rashba effect, and the Heyd-Scuderia-Ernzerhof (HSE06) hybrid functional [46] was further adopted to obtain more accurate values of band gaps. The kinetic pathways of the FE state transformations were calculated by the climbing image nudged elastic band (CINEB) method [47]. MCU code [48] was used for generating 2D images of spin texture and band splitting. The calculation of spin Hall conductivity (SHC) was performed by VASP and WANNIER90 packages [49]. The vdW magnetic tunnel junctions (MTJs) were built by a GaTe/α-In_2Se_3 heterobilayer sandwiched between bottom and top MTJ $MnSe_2$ electrodes. The calculations of spin-transport properties based on MTJs were performed by using DFT coupled with the nonequilibrium Green's function as implemented in the NANODCAL package [50].

III. RESULTS AND DISCUSSION

A. Structural properties of FE heterobilayers

The most common polymorphs of 2D group-III metal chalcogenides are the stoichiometries of M_2X_3 and MX (M = Ga, In and X = S, Se, Te), with respect to an internal atomic layer arrangement of the *X-M-X-M-X* and *X-M-M-X* form, respectively [39]. As a typical example of a M_2X_3 compound, a layered α-In_2Se_3 nanoflake with the space group of $R3m$ has a noncentrosymmetric structure, where the displacement of the Se atom in the middle layer determines the direction of polarization [34]. Its intrinsic out-of-plane electric polarization can persist even at monolayer thickness, as confirmed by experiments [51–53]. For most 2D MX monolayers, their ground state structures exhibit noncentrosymmetry characterized by the $P\bar{6}m2$ space group, while its in-plane spin polarization is largely suppressed due to the horizontal mirror symmetry [54]. Therefore, it is interesting to stack FE α-In_2Se_3 with a MX monolayer together to introduce the symmetry breaking and further facilitate spin splitting [31,32,55]. Furthermore, since the efficient synthesis of MX and α-In_2Se_3 2D nanoflakes, as well as their vdW heterojunctions, has already been demonstrated in experiments [51–53,56–60], the fabrication of MX/α-In_2Se_3 heterostructures is expected to be more readily achievable using mature mechanical assembly methods [61].

As recorded in Table S1 in the SM [42], we find that only the single layers of GaTe and InSe within MX compounds have a perfect lattice match (<1%) with the α-In_2Se_3 monolayer, making it possible to construct the GaTe (InSe)/α-In_2Se_3 heterobilayer in a minimal (1×1) supercell. Although constructing a heterostructure by creating supercells of 2D materials and stacking them with a twisted angle can minimize lattice mismatch, the large size of heterostructure involves many atoms, significantly increasing the computational costs. Therefore, GaTe and InSe are chosen for investigation in this paper.

As shown in Figs. 1(a) and 1(b), two high-symmetry stacking configurations AB and A′B are proposed, of which the A′B configuration can be transformed from AB via counterclockwise rotating the top GaTe (InSe) layer by 60°, as illustrated in Figs. 1(c) and 1(d). Additionally, each stacking have two configurations due to the reversible FE polarization derived from the shift of the central Se layer upward or downward in α-In_2Se_3, denoted as $A^{(')}B$-$FE_{up(down)}$. To examine the structural stability and find the equilibrium interlayer distance, we then calculate the binding energy as the

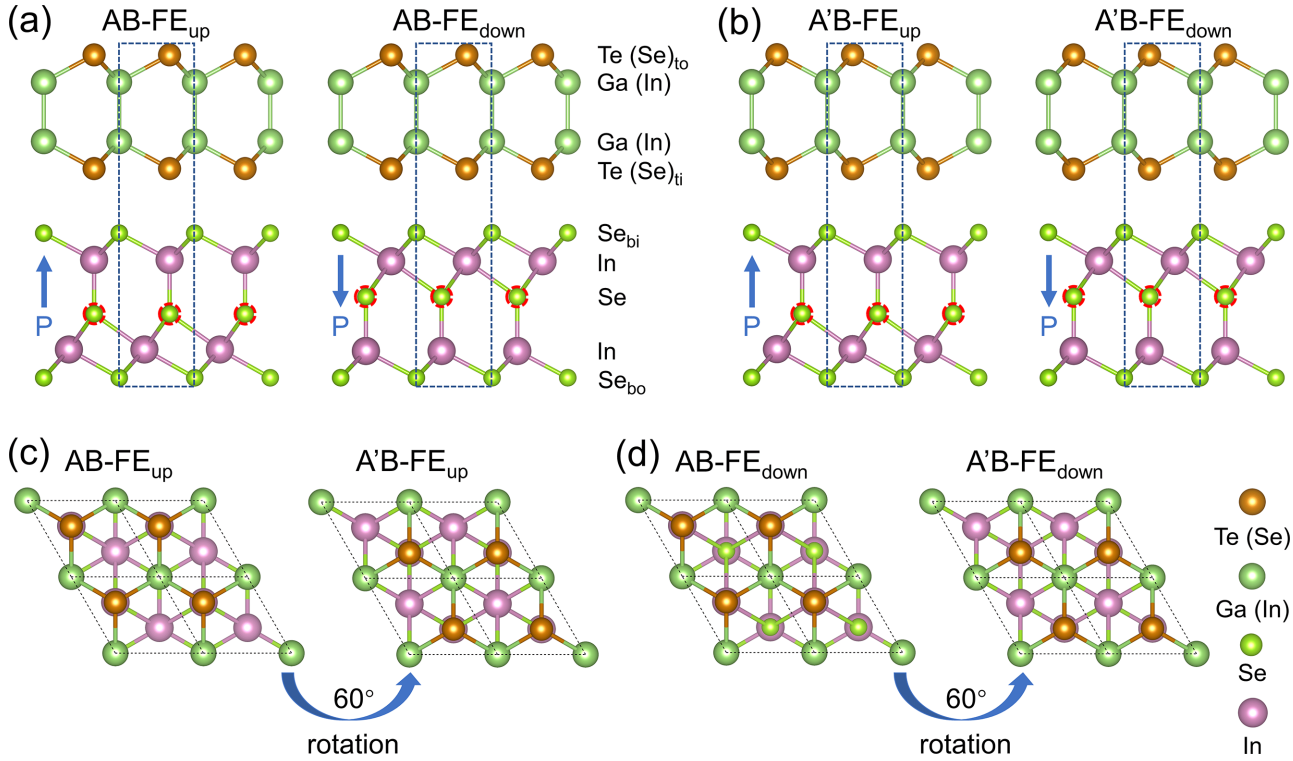

FIG. 1. Side views of two high-symmetry stacking configurations: (a) AB and (b) A′B for GaTe (InSe)/α-In_2Se_3-up(down) heterobilayers, where the displacement of the central Se atom in In_2Se_3 (marked by the red dashed cycle) determines the direction of polarization (indicated by the blue arrow). The unit cell is marked by the blue dash block. Subscripts of to, ti, bi, and bo are used to distinguish outward and interlayer atoms of the top and bottom layers in heterobilayers. (c) and (d) Top views of the relationship between AB and A′B configurations.

following:

$$E_b = \frac{E(\text{hetero}) - E(MX) - E(\alpha\text{-}In_2Se_3)}{S}, \qquad (2)$$

where E(hetero), $E(MX)$, and $E(\alpha$-$In_2Se_3)$ refer to the total energy of the vdW heterostructure, GaTe (InSe) monolayer, and α-In_2Se_3 monolayer, respectively. Here, S is the interfacial area of the heterostructure. According to the definition of Eq. (2), a more negative binding energy indicates a stronger interaction between the structures, and the stacking is more stable. The binding energy as a function of interlayer distance and the fitting results are shown in Fig. S1 in the SM [42]. The calculated binding energy for both GaTe/α-In_2Se_3 and InSe/α-In_2Se_3 range from -18.0 to $-21.3\,\text{meV/Å}^2$, with merely a minimal difference between AB and A′B configurations (see Table I). Meanwhile, these heterobilayers favor the A′B configuration regardless of the polarization direction. There is a relative decrease in interlayer distance and binding energy when switching polarization from the up to down direction, probably indicating the stronger interlayer coupling for the A$^{(')}$B-FE$_{down}$ case. The calculated binding energy values are of the same order of magnitude as typical vdW layered compounds [62], for instance, $-11.86\,\text{meV/Å}^2$ for the Cs_2O monolayer [63] and $-18.2\,\text{meV/Å}^2$ for InSe/GeSe vdW heterostructures [64], indicating that both stacking ways could be thermodynamically stable and obtained in experiments.

TABLE I. The equilibrium interlayer distance (d_e) and the corresponding binding energy (E_b).

Systems	AB configuration		A′B configuration	
	d_e (Å)	E_b (meV)	d_e (Å)	E_b (meV)
GaTe/α-In_2Se_3-up	3.16	−18.6	3.09	−19.2
GaTe/α-In_2Se_3-down	3.07	−20.6	3.0	−21.3
InSe/α-In_2Se_3-up	3.0	−18.0	2.94	−18.4
InSe/α-In_2Se_3-down	2.94	−19.1	2.88	−19.6

To evaluate the energy barrier for the polarization switch between FE$_{up}$ and FE$_{down}$ states in the heterobilayers, we performed CINEB calculations to investigate the kinetic pathways of the polarization reversal processes. As shown in Fig. S2(a) in the SM [42], the barrier values are 0.27 and 0.22 eV per unit cell for GaTe/α-In_2Se_3 and InSe/α-In_2Se_3, respectively, which are close to the values for the pristine α-In_2Se_3 monolayer and Bi(111) bilayer/α-In_2Se_3 heterostructure [34,65]. Given that the FE switch by an external electric field has been experimentally confirmed in pristine α-In_2Se_3 films [35], it is expected that the reversal of the polarization can also be realized in GaTe/α-In_2Se_3 and InSe/α-In_2Se_3 heterobilayers.

B. Electronic properties of FE heterobilayers

First, we study the band structures of pristine GaTe, InSe, and α-In_2Se_3 monolayers with and without SOC as the

TABLE II. The band gap values, Rashba parameters and fitted SOC parameters of the LCBs around Γ for selected 2D materials. Rashba parameter $\alpha_R = 2E_R/k_R$, where E_R is Rashba energy and k_R is the momentum offset. SOC parameters α and β in Eqs. (3) and (6) are obtained from numerical fitting DFT band structures around Γ. NG means negligible values beyond the DFT computational accuracy or the not given values in Eqs. (3) and (6).

Systems	Band gap (eV)	α_R (eV Å)	α (eV Å)	β (eV Å)
α-In_2Se_3	0.75	0.097	0.175	0.008
GaTe	1.29	NG	NG	5.658
InSe	1.32	NG	NG	1.636
GaTe/α-In_2Se_3-up	0.75	0.721	0.857	1.685
GaTe/α-In_2Se_3-down	0.14	0.298	0.375	1.869
InSe/α-In_2Se_3-up	0.51	0.037	0.127	1.321
InSe/α-In_2Se_3-down	0.36	0.077	0.14	1.582

references. As presented in Fig. S3 in the SM [42], the lowest CBs (LCBs) for both GaTe and InSe are twofold degenerate at Γ, while for α-In_2Se_3, they exhibit spin splitting of the double-parabolic feature as normally observed in the typical Rashba-type SOC system, arising from the noncentrosymmetric FE structure. The valence band maxima (VBMs) for three monolayers (GaTe, InSe, and α-In_2Se_3) are located between Γ-K or M-Γ, thus resulting in the indirect band gaps of 1.29, 1.32, and 0.75 eV, respectively (see Table II). As aforementioned, stacking together may facilitate spin splitting, and we then adopt GaTe/InSe and α-In_2Se_3 to construct the FE heterobilayers.

To investigate the Rashba spin splitting in heterobilayers, the corresponding band structures with and without SOC are calculated and shown in Figs. 2(a)–(2d). Overall, GaTe/α-In_2Se_3 systems have enhanced splitting compared with the pristine monolayers, and polarization will control the band splitting significantly. Taking the GaTe/α-In_2Se_3-up-based heterobilayer as an example, one can easily find the dominated contribution of α-In_2Se_3 at the CB minimum (CBM or CB1), which can be attributed to the straddled (type-I) band alignment (see Fig. S4 in the SM [42]). Intriguingly, the band splitting of CB1 is conspicuous when SOC is switched on, as illustrated in Fig. 2(a). After reversing the direction of polarization, the CBM of the α-In_2Se_3-down monolayer becomes lower than the VBM of the GaTe monolayer (see Fig. S4 in the SM [42]), leading to type-III band alignment. As a result, electrons will easily transfer from the GaTe to α-In_2Se_3 layer within the heterostructure, and accordingly, the energy levels of α-In_2Se_3 move downward, while those of GaTe move upward, leading to a noticeable reduction of the band gap, as shown in Fig. 2(b). Using Eq. (1) as the fitting formula, it is found that α_R values are seven times and three times larger than that of the intrinsic α-In_2Se_3 monolayer for up and down polarization states, respectively, highly reflecting the FE manipulation. We attribute the smaller α_R of the down-polarization state to the compensating interfacial electric field, which will be discussed in Sec. III D.

Unlike GaTe/α-In_2Se_3-up, InSe/α-In_2Se_3-up has type-II band alignment (see Fig. S4 in the SM [42]), and it has strong interlayer hybridization at CBM (CB1), which shows small splitting since the contribution of InSe dominates. Although tiny, such splitting is still larger than that of pristine InSe. Upon switching the polarization from up to down, the heterostructure retains a staggered band alignment, but α-In_2Se_3 now dominates the CBM, which induces comparable splitting with pristine α-In_2Se_3. For FE heterobilayers, we also plot the spin distributions in Figs. 2(e)–(2h), which show the out-of-plane distribution and in-plane clockwise/anticlockwise rotation.

C. k·p Hamiltonian analysis

For pristine MX and α-In_2Se_3 monolayers, one can find the different band splitting and spin distribution, as shown in Fig. S3 in the SM [42]. Except the in-plane helical spin texture, one can also find the out-of-plane component (S_z) in the heterobilayers (see Figs. 2(e)–2(h) and S5 in the SM [42]). To better understand these phenomena, we then turn to the symmetry analysis and **k·p** Hamiltonian near Γ.

The MX monolayer possesses D_{3h} point group symmetry, comprising C_{3v} point group symmetry and a mirror reflection (M_h) symmetry with respect to the hexagonal plane, while the α-In_2Se_3 monolayer exhibits only C_{3v} symmetry with the absence of mirror symmetry. For a 2D system with C_{3v} symmetry, the **k·p** Hamiltonian around Γ subjected to SOC can be expressed as [66,67]

$$H(k) = H_0(k) + \alpha k(\cos\theta\sigma_y - \sin\theta\sigma_x) + \beta k^3 \cos(3\theta)\sigma_z, \tag{3}$$

where $H_0(k)$ is the free electron Hamiltonian and σ_i ($i = x, y, z$) are the Pauli matrices. We set $k = \sqrt{k_x^2 + k_y^2}$, in which k_x and k_y are the wave vectors in x (Γ-K) and y (Γ-M) directions, respectively. Here, $\theta = \arctan(k_y/k_x)$ is the angle of momentum k with respect to the x axis. Here, the second (third) term is the Rashba (warping) term, characterized by the Rashba (warping) parameter α (β), which directly relates to the in-plane (out-of-plane) spin texture. Accordingly, the C_{3v} symmetry leads to the band splitting:

$$\Delta E(k,\theta) = [\alpha^2 k^2 + \beta^2 k^6 \cos^2(3\theta)]^{1/2}, \tag{4}$$

and spin polarization:

$$P_{\pm}(k,\theta) = \Delta E(k,\theta)^{-1}[\pm\alpha\cos\theta, \mp\alpha\sin\theta, \mp\beta\cos(3\theta)], \tag{5}$$

where the subscripts + and − represent the bands splitting with higher and lower energies, respectively. However, for the MX monolayer with D_{3h} symmetry, the Rashba term in $H(k)$

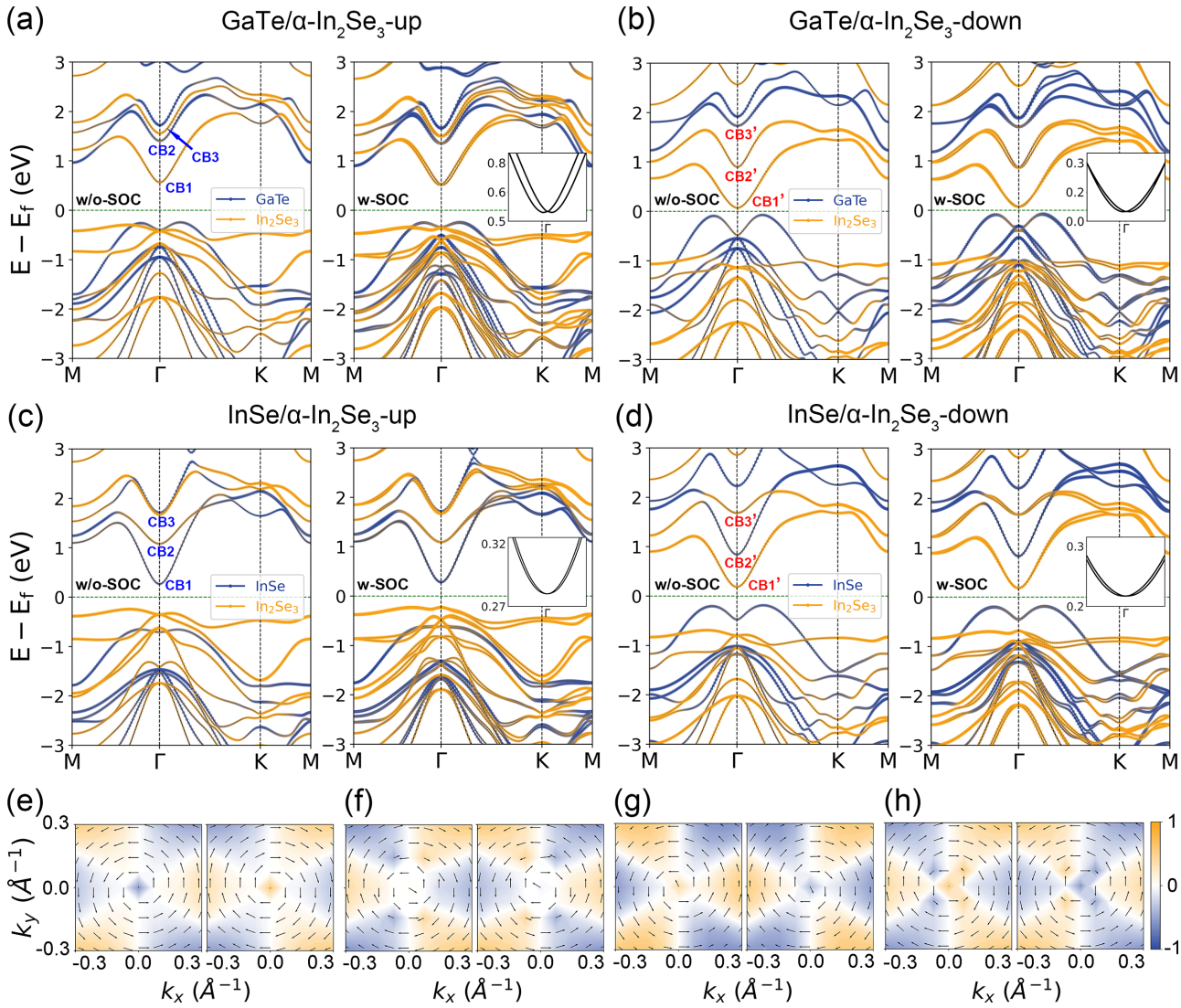

FIG. 2. (a) and (b) Band structures of GaTe/α-In_2Se_3 heterobilayers without (left plane) and with spin-orbit coupling (SOC; right plane). (c) and (d) are the same as (a) and (b), except that they are for InSe/α-In_2Se_3 heterobilayers. Inset: Enlarged view of specific conductor bands around Γ. The size of the circles is proportional to the contribution of atoms. The Fermi level is set to zero and marked by a green dashed line. (e)–(h) Two-dimensional (2D) spin textures of Rashba bands corresponding to the conduction band minimum (CBM) in (a)–(d), respectively. The arrows and color projection represent the in-plane and out-of-plane components of the spin texture with respect to the k_x−k_y plane.

is suppressed by the additional M_h symmetry [68], and hence, the effective Hamiltonian is described by [67]

$$H(k) = H_0(k) + \beta k^3 \cos(3\theta)\sigma_z, \tag{6}$$

which leads to the band splitting:

$$\Delta E(k,\theta) = |\beta k^3 \cos(3\theta)|, \tag{7}$$

and yields a fully out-of-plane spin polarization:

$$P_{\pm}(k,\theta) = \Delta E(k,\theta)^{-1}[0, 0, \mp\beta\cos(3\theta)]. \tag{8}$$

According to Eqs. (4) and (7), the band splitting is expected to be minimum when $\theta = (2n+1)\pi/6$, while the largest ΔE occurs for $\theta = n\pi/3$ ($n \in \mathbb{N}_0$). Using the LCBs for the GaTe monolayer as an example, the vanished band splitting is observed along the high-symmetry line Γ-M, while significant splitting is observed along the Γ-K line, as shown in Fig. 3(a). As also illustrated in Fig. S3(c) in the SM [42], GaTe only has an S_z component, and the in-plane spin textures nearly vanish, basically consistent with the results of our effective Hamiltonian with D_{3h} symmetry [see Eqs. (6)–(8)]. Differently, the α-In_2Se_3 monolayer has small splitting along the Γ-M line due to the decreased symmetry [see Fig. 3(b)]. Additionally, in-plane Rashba helical spin textures can be observed, along with the threefold symmetric distribution of S_z, as displayed in Fig. S3(g) in the SM [42], conforming to Eq. (5).

By constructing heterobilayers, the M_h and inversion symmetries can be disrupted, leading to an out-of-plane potential gradient asymmetry and creating an interfacial electric field along the z direction [31,32,69]. Therefore, constructing MX/α-In_2Se_3 heterobilayers is expected to enhance out-of-plane potential gradient asymmetry by both breaking the mirror symmetry of the MX layer and changing the intrinsic out-of-plane electric field in α-In_2Se_3. This effectively lifts the spin degeneracy of the energy bands around Γ, leading to a

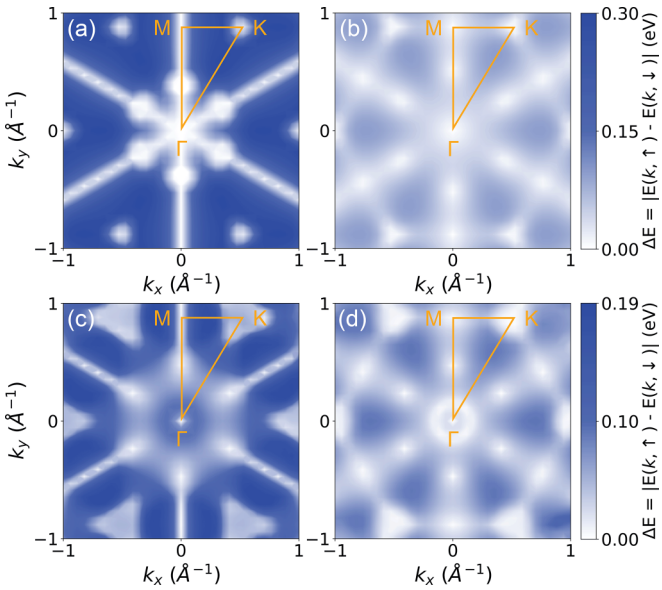

FIG. 3. Contour plots of the spin-splitting energy for the lowest conduction bands (LCBs) of (a) GaTe monolayer, (b) α-In_2Se_3 monolayer, (c) GaTe/α-In_2Se_3-up, and (d) GaTe/α-In_2Se_3-down heterobilayers. The high-symmetry paths in the Brillouin zone are marked by yellow lines.

larger Rashba spin splitting. Due to the broken M_h symmetry, MX/α-In_2Se_3 heterobilayers also exhibit C_{3v} symmetry with a similar formula to the effective Hamiltonian in Eq. (3). Accordingly, similar spin polarization and band splitting to the α-In_2Se_3 monolayer are expected according to Eqs. (4) and (5). Indeed, we already show the coexistence of in-plane helical and out-of-plane spin polarizations in Figs. 2(e)–(2h). As shown in Figs. 3(c) and 3(d), the band splitting behaviors of FE heterobilayers have the same symmetric distribution as the α-In_2Se_3 monolayer when subjected to C_{3v} symmetry. It is important to note that now the Rashba term includes both the intrinsic part of the α-In_2Se_3 monolayer and the extrinsic part induced by breaking the horizontal mirror symmetry of the *MX* monolayer, and this can be manifested by the small but nonnegligible contribution of the *MX* monolayer at the CBM [see Figs. 2(a)–(2d)].

With the effective Hamiltonian, one can have a better understanding of the electronic properties. To determine the strengths of in-plane (dependent on the warping term in the Hamiltonian) and out-of-plane (dependent on the Rashba term in the Hamiltonian) potential gradient asymmetries in different heterobilayers, we then performed numerical fitting of the DFT computed LCBs around Γ by using Eqs. (4) and (7), with the fitted SOC parameters α and β listed in Table II. Basically, these fitted values α for GaTe (InSe)/α-In_2Se_3 heterobilayers are close to the α_R values calculated by using Eq. (1). From the comparison of the fitted SOC parameters (α and β), we notice that, in GaTe/α-In_2Se_3 heterobilayers, both the effective in-plane and out-of-plane potential gradients are much enhanced compared with those in pristine α-In_2Se_3.

D. Mechanism of Rashba spin splitting in FE heterobilayers

As mentioned above, the Rashba term is related to the out-of-plane potential gradient asymmetry, and thus, it is more sensitive to the p_z orbital. The partial density of states (PDOS) and orbital-projected band structures are then investigated for GaTe (InSe)/α-In_2Se_3-up/down heterobilayers, respectively, as shown in Fig. 4. From the calculated PDOS [see Figs. 4(a)–(4d)], it is obvious that the unoccupied states near the Fermi level are mainly dominated by *p* orbitals of chalcogen atoms hybridized with *s* orbitals from metal atoms. Note that the contributions of *s* orbitals are always smaller than the dominated orbitals, and the *s* orbital is nondirectional in the spherically symmetric shape; hence, only *p* orbitals are considered herein. In fact, CB1$^{(\prime)}$, CB2$^{(\prime)}$, and CB3$^{(\prime)}$ around Γ are all dominated by the p_z orbital of interfacial chalcogen atoms, while contributions from p_x and p_y orbitals are quite limited (see Figs. 4(e)–4(h) and S7(d)–S7(g) in the SM [42]), which implies that symmetry breaking indeed facilitates the interlayer interaction/polarization mainly through the p_z orbital. Taking GaTe/α-In_2Se_3-up as an example, it is easy to find that the major contributions to the CBM come from the p_z orbitals of interlayer Te_{ti} and Se_{bi} atoms.

To further reveal the spin-electric coupling mechanism deriving from the interplay between interfacial interaction and FE polarization, the charge density difference is calculated to directly reflect the interfacial charge redistribution. As shown in Fig. 5, the charge depletion occurs near the GaTe (InSe) layer, indicating a downward interfacial electric field (E_i). As a result, E_i will keep the opposite direction compared with the built-in electric field of the α-In_2Se_3 layer (E_s) when polarization is downward, forming charge screening, whilst enhancing the total electric field when the polarization is upward. Correspondingly, Rashba spin splitting is expected to be enhanced and suppressed for the FE_{up} and FE_{down} cases, respectively. Indeed, as listed in Table II, the magnitude of the overall spin splitting in GaTe/α-In_2Se_3-up is larger than that of GaTe/α-In_2Se_3-down. Nevertheless, the splitting magnitudes are distinctly stronger than that of pristine α-In_2Se_3.

Compared with InSe/α-In_2Se_3 heterobilayers, the most noticeable difference is that a distinct charge transfer appears at the interface of the GaTe/α-In_2Se_3 heterobilayers, as shown in Fig. 5, which can be explained by the different electronegativity values of the Se (2.55) and Te (2.10) atoms. Such a disparity induces directional charge transfer from the side of the Te_{ti} atom to the side of Se_{bi}, resulting in a relatively stronger E_i. This also explains why the out-of-plane potential gradient asymmetry in GaTe/α-In_2Se_3 is more pronounced than in InSe/α-In_2Se_3 heterobilayers. On account of the nonzero E_i and the increased E_s perpendicular to the heterostructure $\langle Te_{ti} - p_z|E_i|Te_{ti} - p_z\rangle \neq 0$ and $\langle Se_{bi} - p_z|E_s|Se_{bi} - p_z\rangle \neq 0$, considerably enhanced Rashba spin splitting can be observed at the CBM of GaTe/α-In_2Se_3-up, based on the form of the orbital Rashba effect [9]. A more pronounced charge transfer is evident in GaTe/α-In_2Se_3-down, indicating the increased intensity of E_i. However, as opposed to the direction of E_s, the resulting Rashba splitting for GaTe/α-In_2Se_3-down is suppressed. For InSe/α-In_2Se_3 heterobilayers, the CBs around Γ merely exhibit weak spin splitting due to either a negligible E_i or the interfacial charge screening. In general, reasonable agreement is found between the Rashba parameters in Table II.

The above mechanism of FE manipulation of spin splitting can also be applied to other vdW heterostructures with the

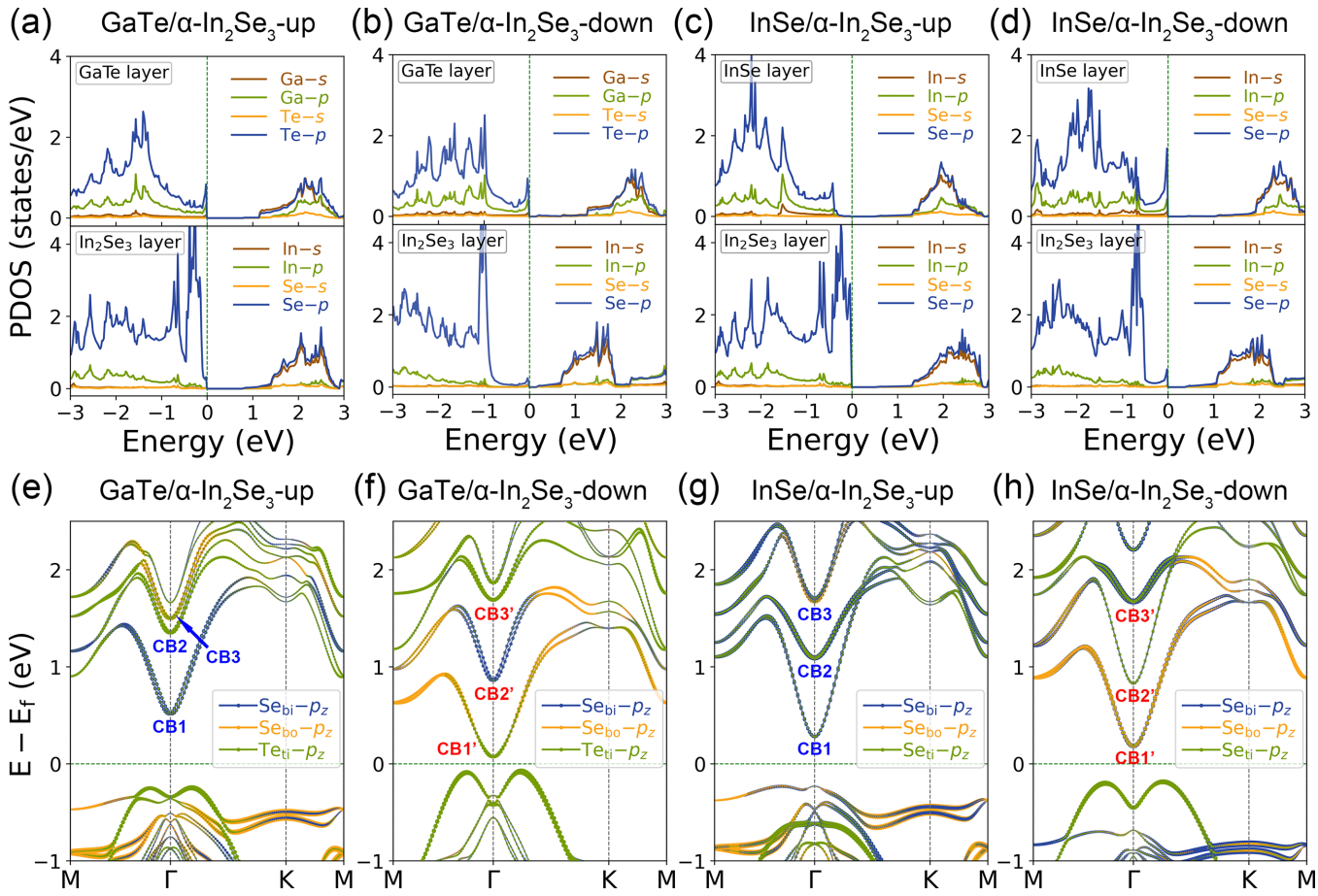

FIG. 4. (a)–(d) The partial density of states (PDOS) and (e)–(h) atom-projected bands of GaTe/α-In_2Se_3 and InSe/α-In_2Se_3 heterobilayers. The size of the circles is proportional to the contribution of orbitals. The Fermi level is set to zero and marked by green dashed line.

same point group symmetry. For example, we have tested heterostructures constructed by *MX* and bilayer α-In_2Se_3 (see Fig. S6 in the SM [42]) as well as heterobilayers combined with the III-VI group (α phase) and α-In_2Se_3. As shown in Table S2 in the SM [42], GeSb/α-In_2Se_3 heterobilayers are predicted to be semiconductors with a large Rashba parameter (α_R) of 0.715 and 1.235 (eV Å) under the FE_{up} and FE_{down} states, respectively.

E. Electronic properties of α-In_2Se_3/GaTe/α-In_2Se_3 sandwiched heterostructures

The magnitude of stacking-induced Rashba SOC can be controlled by adjusting the twist angle, as demonstrated in the graphene/TMDs and WSe_2/phosphorene/WSe_2 heterostructures, where the obvious splitting is evident in an asymmetrically stacked configuration [70,71]. Herein, the electronic properties of α-In_2Se_3/GaTe/α-In_2Se_3 sandwiched heterostructures are then investigated, in which we will show that the direction of FE polarization is another degree of freedom to manipulate the spin splitting and Rashba SOC.

As shown in Figs. S8(a)–S8(c) in the SM [42], by switching the direction of polarization in the top and bottom α-In_2Se_3 layers, four structural states can be constructed: P1 (head-to-head), P2 (head-to-tail), P3 (tail-to-head), and P4 (tail-to-tail). In both ABA and A′BA′ stacking configurations, P1 and P4 states are antiferroelectric and belong to the $P\bar{6}m2$ space group, while P2 and P3 states are FE and belong to the $P3m1$ space group. Interestingly, the FE polarization reversal in α-In_2Se_3/GeTe/α-In_2Se_3 heterostructures, such as P1 to P2/P3 (P2/P3 to P4), experience smaller energy barriers of 0.16 (0.13) eV per unit cell compared with the direct FE switch in GaTe/α-In_2Se_3 heterobilayers (see Fig. S2 in the SM [42]), indicating the feasible switch. Next, we will take the A′BA′ stacked configurations as examples to explore the detailed electronic properties, and other sandwiched structures belonging to the ABA/ABA′ stacked configuration are summarized in Figs. S8(d) and S8(e) in the SM [42].

The band structures of the P1–P4 states are summarized in Fig. 6(a). Clearly, P1 possesses the largest band gap, while P2/P3 have a smaller one, and P4 appears to be metallic. According to the HSE06 calculations, P4 has a small indirect gap of 0.12 eV. Such a tendency can be understood by the charge redistribution between GaTe and the top/bottom α-In_2Se_3 layers [see Fig. 6(e)]. As compared with P1, more electrons are transferred from the GaTe layer to the bottom (top) α-In_2Se_3 layer in P2 (P3). This unequal charge redistribution drives the CBM downward and pushes the VBM upward, causing the decrease of the band gap, while for P4, the pronounced interfacial charge transfer further leads to the decrease band gap.

Furthermore, details of CBs are presented to elucidate the associated effect on the Rashba splitting. According to the symmetry arguments, P1 and P4 belong to the symmetry

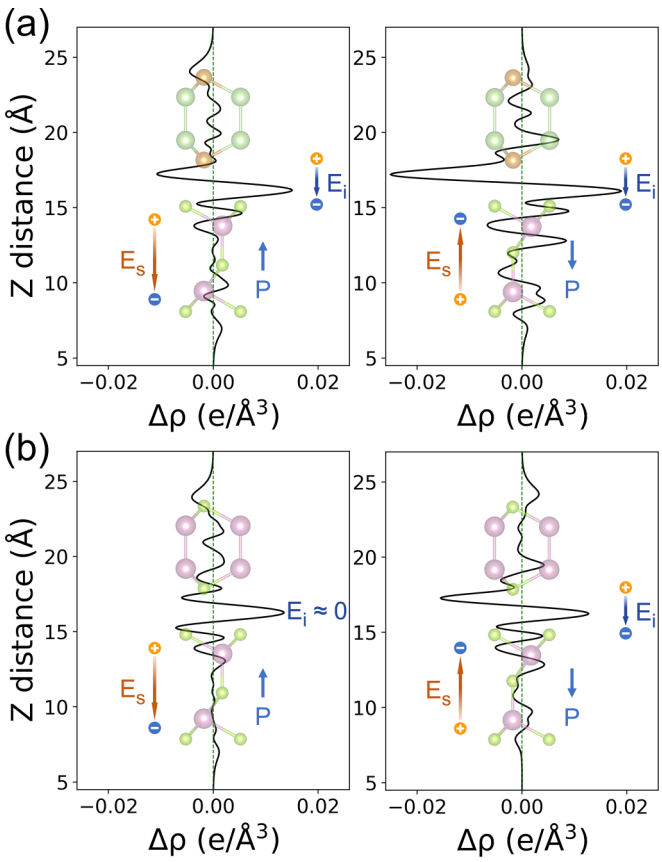

FIG. 5. (a) Plane-averaged charge density difference along the z direction for GaTe/α-In_2Se_3-up (left panel) and down (right panel). (b) is the same as (a), except that it is for InSe/α-In_2Se_3 heterobilayers. Here E_s and E_i represent the built-in electric field and the charge redistribution induced interfacial electric field, respectively.

point group of D_{3h}, while P2 and P3 belong to C_{3v}. Therefore, their effective Hamiltonians around Γ should be the same as MX and α-In_2Se_3, respectively. Accordingly, similar band splitting and spin distributions are expected. P1 and P4 have the twofold degeneracy on each CB near Γ, but in stark contrast, $P3m1$ space group (C_{3v}) symmetry breaks M_h symmetry and induces spin splitting in the P2 and P3 configurations, as illustrated in Fig. 6(a). Intuitively, P2/P3 can be viewed as the effective composition of GaTe/α-In_2Se_3-up and GaTe/α-In_2Se_3-down even though there is only one GaTe layer. As a result, the overall SOC-induced spin splitting of P2/P3 is compromised, and the DFT calculated α_R is 0.359 eV Å, which is close to the averaged values of both GaTe/α-In_2Se_3-up and down (0.51 eV Å; see α and β values in Tables II and III). Additionally, the in-plane spin textures with clockwise and anticlockwise spin polarizations are observed in the P2/P3 configurations around Γ, which are the typical features of Rashba spin splitting. However, these in-plane textures vanish in both the P1 and P4 configurations, where out-of-plane spin polarizations dominate, like the results reported in WSe_2/phosphorene/WSe_2 heterostructures [71]. The symmetric and asymmetric distributions of the out-of-plane potential gradient for all configurations are also manifested by the plane-averaged electron density difference in Fig. 6(e), aligning well with the magnitudes of the numerically fitted SOC parameters listed in Table III. It is evident that the out-of-plane potential gradient asymmetry can be strongly suppressed by M_h symmetry, hence yielding an evident out-of-plane spin polarization.

TABLE III. The DFT calculated Rashba parameters α_R and fitted SOC parameters α and β of the LCBs around Γ for α-In_2Se_3/GaTe/α-In_2Se_3 sandwich heterostructures.

Configurations	Polarization states	α_R (eV Å)	α (eV Å)	β (eV Å)
ABA	P1	NG	NG	3.57
	P2/P3	0.319	0.399	0.716
	P4	NG	NG	3.824
ABA′	P1	0.238	0.377	0.794
	P2	0.332	0.415	0.762
	P3	0.36	0.466	0.794
	P4	0.365	0.432	−0.685
A′BA′	P1	NG	NG	6.541
	P2/P3	0.359	0.355	−0.913
	P4	NG	NG	6.589

For ABA′ stacking, where the top/bottom α-In_2Se_3 monolayer is twisted by 0° or 60° with respect to the middle GaTe monolayer (see Fig. S8(c) in the SM [42]), all the heterostructures (P1–P4) now belong to the $P3m1$ space group and have C_{3v} symmetry. Hence, the SOC-induced spin splitting of CBs around Γ is observed, as illustrated in Fig. S8(e) in the SM [42] and supported by the DFT-calculated α_R and fitted α values in Table III.

These findings demonstrate that FE polarization can effectively tune band splitting in sandwiched heterostructures, and the large interfacial interaction can significantly enhance the Rashba SOC when M_h symmetry is broken.

F. FE manipulation of spin-transport properties

From the perspective of practical applications, FE manipulation of spin-transport properties is of great significance, including SHC and spin current. For example, the combination of high charge mobility and moderate SOC can lead to a gate-tunable SHE in a graphene/WS_2 heterostructure device [72]. To investigate the FE control of the SHE, the SHCs of both the heterobilayer and sandwiched heterostructure (A′BA′ stacked configuration) are calculated based on GaTe and α-In_2Se_3, as plotted in Fig. 7.

As shown in Fig. 7(a), a noticeable negative peak emerges in the vicinity of the CBM in GaTe/α-In_2Se_3-up, which is nearly absent in both the pristine monolayer of In_2Se_3 and GaTe. This behavior is attributed to the enhanced Rashba spin splitting of CB1. Similarly, a peak is located at the higher energy above CBM for the FE_{down} heterobilayer, which arises from the band splitting of CB2′. This discrepancy in SHC with respect to polarization direction stems from the interfacial charge redistribution, and the regulation of SHC is determined by the interplay between the intrinsic Rashba SOC from FE polarization and E_i from interfacial charge transfer, especially evident in the α-In_2Se_3/GaTe/α-In_2Se_3 sandwiched heterostructure. A small negative peak at $E = 0.7$ eV only appears in P2/P3, attributed to Rashba SOC with the reduced symmetry. Additionally, a negative peak around $E = 1$ eV appears in all configurations, and the magnitude

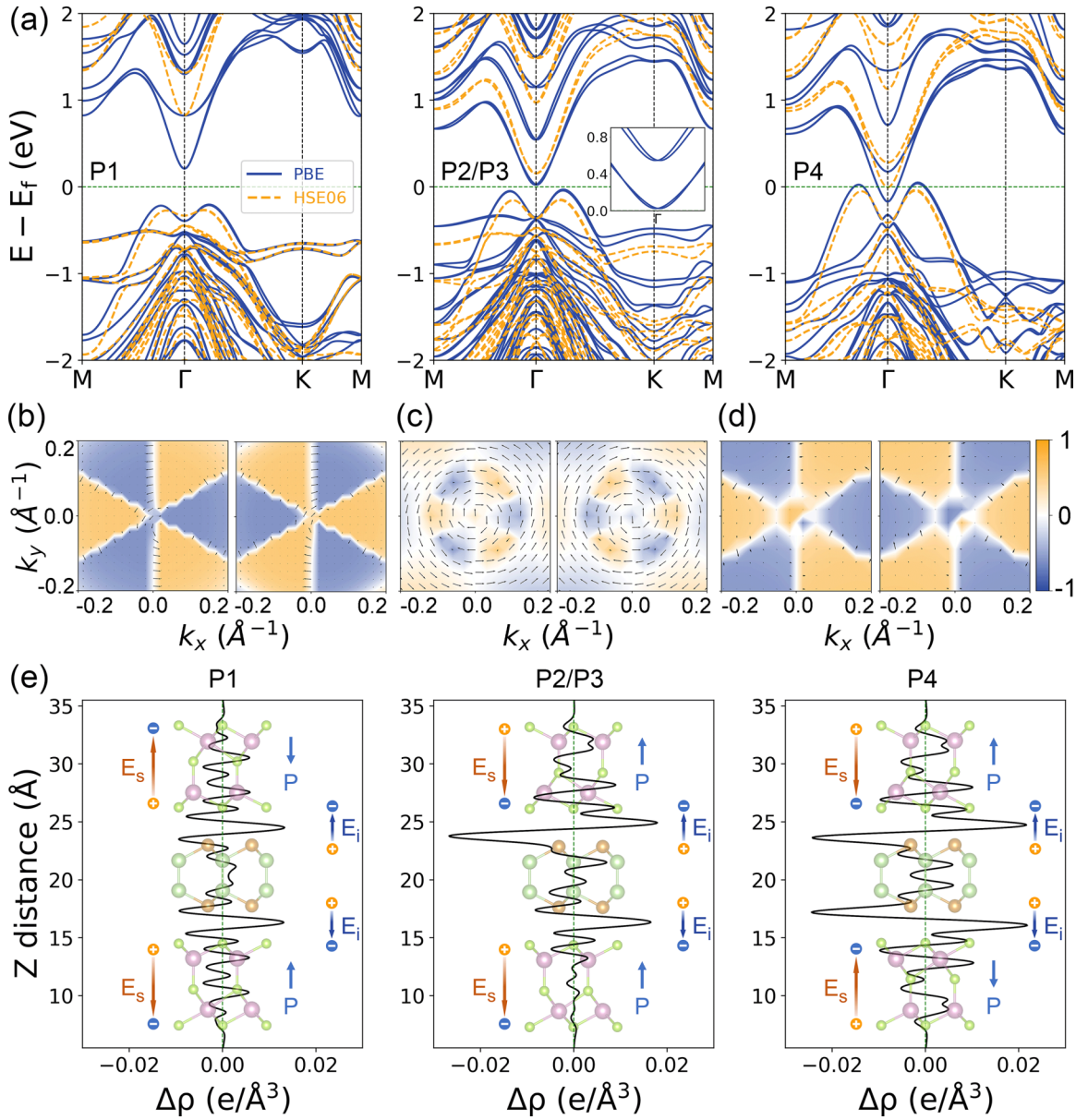

FIG. 6. (a) Band structures of α-In_2Se_3/GaTe/α-In_2Se_3 heterostructures with A′BA′ stacking configuration. The Fermi level is set to zero and marked by green dashed line. Inset in (a): Enlarged view of specific conductor bands around Γ. (b)–(d) Two-dimensional (2D) spin textures of the lowest conduction bands (LCBs) around Γ corresponding to P1, P2/P3, and P4 states, respectively. The arrows and color projection follow the definitions in Fig. 2. (e) Plane-averaged charge density difference along the z direction.

of SHC (P2/P3 > P4 > P1) is correlated with the interfacial charge redistribution [see Fig. 6(e)]. It is also noticeable to find that SHC of VBs is larger than CBs. For example, SHC peaks near $E = -1$ eV for the α-In_2Se_3 monolayer are strongly enhanced when the heterobilayer is formed due to the interfacial E_i and charge transfer. Similarly, the behavior of this peak in the sandwiched heterostructures conforms to the interlayer interactions in Fig. 6(e).

We further investigate the tunneling properties in MTJs based on the FE heterobilayers. As plotted in Fig. 7(b), the metallic $MnSe_2$ monolayer with ferromagnetism is taken as the magnetic electrode, and the FE-controlled MTJ, i.e., $MnSe_2$/GaTe/α-In_2Se_3/$MnSe_2$, is constructed. First, the SOC effect is excluded to investigate the FE manipulation in Fig. S9 in the SM [42]. Clearly, the spin-up and down configurations give the different transmission for FE_{up} and FE_{down} states. For example, a transmission peak can be found near the Fermi level for FE_{down} in the spin-up channel, while the transmission nearly vanishes for the FE_{up} case, demonstrating the effective FE regulation. The FE control can also be visualized near $E = -1$ eV, where the dominating spin component reverses. When the SOC effect is accounted, as depicted in Fig. 7(c), the spin channels are entangled, and the total transmission is significantly enlarged compared with the single-spin cases. Intriguingly, the FE regulation phenomenon is also observed, and the switchable behavior can be found at the whole energy region, suggesting the potential application in multifunctional nanospintronics through FE switching.

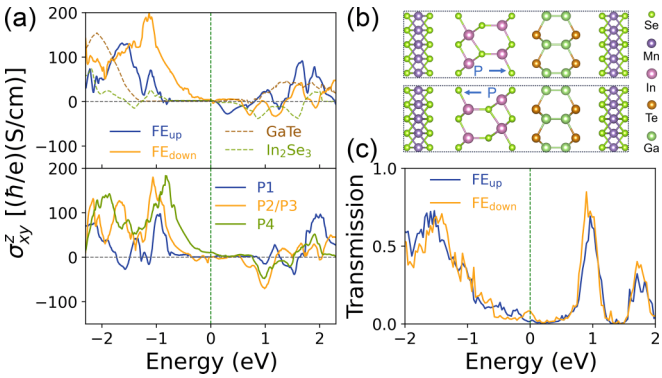

FIG. 7. (a) Calculated spin Hall conductivity. Up panel: GaTe/α-In_2Se_3 heterobilayers (FE_{up} and FE_{down}) and pristine monolayers. Bottom panel: α-In_2Se_3/GaTe/α-In_2Se_3 (A′BA′ stacked configuration) heterostructures (P1–P4). The conduction band minimum (CBM) is set to zero and marked by green dashed line. (b) Side views of $MnSe_2$/GaTe/α-In_2Se_3/$MnSe_2$ magnetic tunnel junctions (MTJ) with upward and downward ferroelectric (FE) polarizations. (c) The zero-bias transmission curves when spin-orbit coupling (SOC) is considered. The Fermi level is set to zero and marked by green dashed line.

IV. CONCLUSIONS

In summary, we propose an effective approach to simultaneously realize FE manipulation and enhancement of spin splitting in the 2D vdW heterostructures. Such an enhancement originates from the increased intensity of the effective electric field due to the interfacial charge transfer. Notably, significantly enhanced Rashba parameters (α_R) of 0.721 and 0.298 eV Å are observed in the GaTe/α-In_2Se_3 heterobilayer under the FE_{up} and FE_{down} states, respectively, compared with 0.097 eV Å in the α-In_2Se_3 monolayer. Furthermore, α-In_2Se_3/GaTe/α-In_2Se_3 sandwiched structures are explored for the purpose of multilevel FE manipulation of spin splitting, and it is demonstrated that the spin-transport properties including SHC and MTJ transmission can be effectively regulated by the FE switch. Overall, our findings highlight the potential of 2D vdW heterostructures as an appealing platform for designing FE Rashba semiconductors with large spin splitting and enabling further applications in nanoelectronics and spintronics.

ACKNOWLEDGMENTS

This paper is supported by the Photon Science Center for Carbon Neutrality of Chinese Academy of Sciences, National Natural Science Foundation of China (Grant No. 12204029), the Natural Science Foundation of Zhejiang Province (Grants No. LY23E020010 and No. LQ23A040013), and the funding of "Leading Innovative and Entrepreneur Team Introduction Program of Zhejiang" (Grant No. 2020R01002). Y.W. also acknowledges the funding from China Postdoctoral Science Foundation (Grant No. 2023M743098).

[1] J. Wunderlich, B. Kaestner, J. Sinova, and T. Jungwirth, Experimental observation of the spin-Hall effect in a two-dimensional spin-orbit coupled semiconductor system, Phys. Rev. Lett. **94**, 047204 (2005).

[2] F. Sheng, C. Hua, M. Cheng, J. Hu, X. Sun, Q. Tao, H. Lu, Y. Lu, M. Zhong, K. Watanabe *et al.*, Rashba valleys and quantum Hall states in few-layer black arsenic, Nature (London) **593**, 56 (2021).

[3] T. Koga, J. Nitta, H. Takayanagi, and S. Datta, Spin-filter device based on the Rashba effect using a nonmagnetic resonant tunneling diode, Phys. Rev. Lett. **88**, 126601 (2002).

[4] J. C. Sanchez, L. Vila, G. Desfonds, S. Gambarelli, J. P. Attane, J. M. De Teresa, C. Magen, and A. Fert, Spin-to-charge conversion using Rashba coupling at the interface between nonmagnetic materials, Nat. Commun. **4**, 2944 (2013).

[5] A. Manchon, H. C. Koo, J. Nitta, S. M. Frolov, and R. A. Duine, New perspectives for Rashba spin-orbit coupling, Nat. Mater. **14**, 871 (2015).

[6] E. Lesne, Y. Fu, S. Oyarzun, J. C. Rojas-Sánchez, D. C. Vaz, H. Naganuma, G. Sicoli, J. P. Attané, M. Jamet, E. Jacquet *et al.*, Highly efficient and tunable spin-to-charge conversion through Rashba coupling at oxide interfaces, Nat. Mater. **15**, 1261 (2016).

[7] P. Noël, F. Trier, L. M. Vicente Arche, J. Bréhin, D. C. Vaz, V. Garcia, S. Fusil, A. Barthélémy, L. Vila, M. Bibes *et al.*, Nonvolatile electric control of spin–charge conversion in a $SrTiO_3$ Rashba system, Nature (London) **580**, 483 (2020).

[8] X. F. Lu, C.-P. Zhang, N. Wang, D. Zhao, X. Zhou, W. Gao, X. H. Chen, K. T. Law, and K. P. Loh, Nonlinear transport and radio frequency rectification in BiTeBr at room temperature, Nat. Commun. **15**, 245 (2024).

[9] G. Bihlmayer, P. Noël, D. V. Vyalikh, E. V. Chulkov, and A. Manchon, Rashba-like physics in condensed matter, Nat. Rev. Phys. **4**, 642 (2022).

[10] H. Yi, L.-H. Hu, Y. Wang, R. Xiao, J. Cai, D. R. Hickey, C. Dong, Y.-F. Zhao, L.-J. Zhou, R. Zhang *et al.*, Crossover from Ising- to Rashba-type superconductivity in epitaxial Bi_2Se_3/monolayer $NbSe_2$ heterostructures, Nat. Mater. **21**, 1366 (2022).

[11] M. S. Hossain, F. Schindler, R. Islam, Z. Muhammad, Y.-X. Jiang, Z.-J. Cheng, Q. Zhang, T. Hou, H. Chen, M. Litskevich *et al.*, A hybrid topological quantum state in an elemental solid, Nature (London) **628**, 527 (2024).

[12] S. Picozzi, Ferroelectric Rashba semiconductors as a novel class of multifunctional materials, Front. Phys. **2**, 10 (2014).

[13] D. Di Sante, P. Barone, R. Bertacco, and S. Picozzi, Electric control of the giant Rashba effect in bulk GeTe, Adv. Mater. **25**, 509 (2013).

[14] M. Liebmann, C. Rinaldi, D. Di Sante, J. Kellner, C. Pauly, R. N. Wang, J. E. Boschker, A. Giussani, S. Bertoli, M. Cantoni *et al.*, Giant Rashba-type spin splitting in ferroelectric GeTe(111), Adv. Mater. **28**, 560 (2016).

[15] C. Rinaldi, S. Varotto, M. Asa, J. Slawinska, J. Fujii, G. Vinai, S. Cecchi, D. Di Sante, R. Calarco, I. Vobornik *et al.*, Ferroelectric control of the spin texture in GeTe, Nano Lett. **18**, 2751 (2018).

[16] X. Yang, X. M. Li, Y. Li, Y. Li, R. Sun, J. N. Liu, X. Bai, N. Li, Z. K. Xie, L. Su *et al.*, Three-dimensional limit of bulk Rashba

effect in ferroelectric semiconductor GeTe, Nano Lett. **21**, 77 (2021).

[17] K. Ishizaka, M. S. Bahramy, H. Murakawa, M. Sakano, T. Shimojima, T. Sonobe, K. Koizumi, S. Shin, H. Miyahara, A. Kimura *et al.*, Giant Rashba-type spin splitting in bulk BiTeI, Nat. Mater. **10**, 521 (2011).

[18] A. Crepaldi, L. Moreschini, G. Autes, C. Tournier-Colletta, S. Moser, N. Virk, H. Berger, P. Bugnon, Y. J. Chang, K. Kern *et al.*, Giant ambipolar Rashba effect in the semiconductor BiTeI, Phys. Rev. Lett. **109**, 096803 (2012).

[19] A. Narayan, Class of Rashba ferroelectrics in hexagonal semiconductors, Phys. Rev. B **92**, 220101(R) (2015).

[20] P. D. C. King, R. H. He, T. Eknapakul, P. Buaphet, S.-K. Mo, Y. Kaneko, S. Harashima, Y. Hikita, M. S. Bahramy, C. Bell *et al.*, Subband structure of a two-dimensional electron gas formed at the polar surface of the strong spin-orbit perovskite $KTaO_3$, Phys. Rev. Lett. **108**, 117602 (2012).

[21] M. Kim, J. Im, A. J. Freeman, J. Ihm, and H. Jin, Switchable $S = \frac{1}{2}$ and $J = \frac{1}{2}$ Rashba bands in ferroelectric halide perovskites, Proc. Natl. Acad. Sci. USA **111**, 6900 (2014).

[22] L. G. D. da Silveira, P. Barone, and S. Picozzi, Rashba-Dresselhaus spin-splitting in the bulk ferroelectric oxide $BiAlO_3$, Phys. Rev. B **93**, 245159 (2016).

[23] B. Zhou, Ferroelectric Rashba semiconductors, $AgBiP_2X_6$ (X = S, Se and Te), with valley polarization: An avenue towards electric and nonvolatile control of spintronic devices, Nanoscale **12**, 5533 (2020).

[24] Y. Wang, Z. Lei, J. Zhang, X. Tao, C. Hua, and Y. Lu, Ferroelectricity and large Rashba splitting in two-dimensional tellurium, Chin. Phys. Lett. **40**, 117102 (2023).

[25] D. Di Sante, A. Stroppa, P. Barone, M.-H. Whangbo, and S. Picozzi, Emergence of ferroelectricity and spin-valley properties in two-dimensional honeycomb binary compounds, Phys. Rev. B **91**, 161401(R) (2015).

[26] E. Bruyer, D. Di Sante, P. Barone, A. Stroppa, M.-H. Whangbo, and S. Picozzi, Possibility of combining ferroelectricity and Rashba-like spin splitting in monolayers of the 1T-type transition-metal dichalcogenides MX_2 (M = Mo, W; X = S, Se, Te), Phys. Rev. B **94**, 195402 (2016).

[27] Z. Lin, C. Si, S. Duan, C. Wang, and W. Duan, Rashba splitting in bilayer transition metal dichalcogenides controlled by electronic ferroelectricity, Phys. Rev. B **100**, 155408 (2019).

[28] C. M. Acosta, A. Fazzio, G. M. Dalpian, and A. Zunger, Inverse design of compounds that have simultaneously ferroelectric and Rashba cofunctionality, Phys. Rev. B **102**, 144106 (2020).

[29] J. Chen, K. Wu, W. Hu, and J. Yang, High-throughput inverse design for 2D ferroelectric Rashba semiconductors, J. Am. Chem. Soc. **144**, 20035 (2022).

[30] S. Gupta and B. I. Yakobson, What dictates Rashba splitting in 2D van der Waals heterobilayers, J. Am. Chem. Soc. **143**, 3503 (2021).

[31] M. J. Szary, M. T. Michalewicz, and M. W. Radny, Giant spin splitting induced by a symmetry-braking van der Waals interaction, Appl. Surf. Sci. **494**, 619 (2019).

[32] Q. Zhang and U. Schwingenschlögl, Rashba effect and enriched spin-valley coupling in GaX/MX_2 (M = Mo, W; X = S, Se, Te) heterostructures, Phys. Rev. B **97**, 155415 (2018).

[33] S. Sattar and J. A. Larsson, Tunable electronic properties and large Rashba splittings found in few-layer Bi_2Se_3/$PtSe_2$ van der Waals Heterostructures, ACS Appl. Electron. Mater. **2**, 3585 (2020).

[34] W. Ding, J. Zhu, Z. Wang, Y. Gao, D. Xiao, Y. Gu, Z. Zhang, and W. Zhu, Prediction of intrinsic two-dimensional ferroelectrics in In_2Se_3 and other III_2-VI_3 van der Waals materials, Nat. Commun. **8**, 14956 (2017).

[35] Y. Zhou, D. Wu, Y. Zhu, Y. Cho, Q. He, X. Yang, K. Herrera, Z. Chu, Y. Han, M. C. Downer *et al.*, Out-of-plane piezoelectricity and ferroelectricity in layered α-In_2Se_3 nanoflakes, Nano Lett. **17**, 5508 (2017).

[36] G. Kresse and J. Furthmuller, Efficient iterative schemes for *ab initio* total-energy calculations using a plane-wave basis set, Phys. Rev. B **54**, 11169 (1996).

[37] J. P. Perdew, K. Burke, and M. Ernzerhof, Generalized gradient approximation made simple, Phys. Rev. Lett. **77**, 3865 (1996).

[38] P. E. Blochl, Projector augmented-wave method, Phys. Rev. B **50**, 17953 (1994).

[39] H. Bergeron, D. Lebedev, and M. C. Hersam, Polymorphism in post-dichalcogenide two-dimensional materials, Chem. Rev. **121**, 2713 (2021).

[40] S. Grimme, J. Antony, S. Ehrlich, and H. Krieg, A consistent and accurate *ab initio* parametrization of density functional dispersion correction (DFT-D) for the 94 elements H-Pu, J. Chem. Phys. **132**, 154104 (2010).

[41] S. Grimme, S. Ehrlich, and L. Goerigk, Effect of the damping function in dispersion corrected density functional theory, J. Comput. Chem. **32**, 1456 (2011).

[42] See Supplemental Material at http://link.aps.org/supplemental/10.1103/PhysRevB.110.085110 for details about the structural and electronic properties of single-layer MX and α-In_2Se_3; fitting curves of interlayer distance and binding energy for GaTe (InSe)/α-In_2Se_3; the kinetic pathway and energy barrier of FE switch; the band gaps and Rashba parameters of selected 2D FE Rashba materials; stacking configurations and band structures of sandwiched heterostructures; the spin-resolved zero-bias transmission curves of MTJ; and which includes Refs. [24,29,39–41,43–45].

[43] J. Klimes, D. R. Bowler, and A. Michaelides, Chemical accuracy for the van der Waals density functional, J. Phys.: Condens. Matter **22**, 022201 (2010).

[44] J.-J. Zhang, D. Zhu, and B. I. Yakobson, Heterobilayer with ferroelectric switching of topological state, Nano Lett. **21**, 785 (2021).

[45] H. Jafari, E. Barts, P. Przybysz, K. Tenzin, P. J. Kowalczyk, P. Dabrowski, and J. Sławińska, Robust Zeeman-type band splitting in sliding ferroelectrics, Phys. Rev. Mater. **8**, 024005 (2024).

[46] M. Marsman, J. Paier, A. Stroppa, and G. Kresse, Hybrid functionals applied to extended systems, J. Phys.: Condens. Matter **20**, 064201 (2008).

[47] G. Henkelman, B. P. Uberuaga, and H. Jónsson, A climbing image nudged elastic band method for finding saddle points and minimum energy paths, J. Chem. Phys. **113**, 9901 (2000).

[48] H. Q. Pham, MCU: Modeling and Crystallographic Utilities, 2021 https://github.com/hungpham2017/mcu (accessed Jan. 18, 2021).

[49] G. Pizzi, V. Vitale, R. Arita, S. Blugel, F. Freimuth, G. Geranton, M. Gibertini, D. Gresch, C. Johnson, T. Koretsune

et al., WANNIER90 as a community code: New features and applications, J. Phys.: Condens. Matter **32**, 165902 (2020).

[50] J. Taylor, H. Guo, and J. Wang, *Ab initio* modeling of quantum transport properties of molecular electronic devices, Phys. Rev. B **63**, 245407 (2001).

[51] J. Xiao, H. Zhu, Y. Wang, W. Feng, Y. Hu, A. Dasgupta, Y. Han, Y. Wang, D. A. Muller, L. W. Martin *et al.*, Intrinsic two-dimensional ferroelectricity with dipole locking, Phys. Rev. Lett. **120**, 227601 (2018).

[52] F. Xue, W. Hu, K.-C. Lee, L.-S. Lu, J. Zhang, H.-L. Tang, A. Han, W.-T. Hsu, S. Tu, W.-H. Chang *et al.*, Room-temperature ferroelectricity in hexagonally layered α-In_2Se_3 nanoflakes down to the monolayer limit, Adv. Funct. Mater. **28**, 1803738 (2018).

[53] C. Cui, W.-J. Hu, X. Yan, C. Addiego, W. Gao, Y. Wang, Z. Wang, L. Li, Y. Cheng, P. Li *et al.*, Intercorrelated in-plane and out-of-plane ferroelectricity in ultrathin two-dimensional layered semiconductor In_2Se_3, Nano Lett. **18**, 1253 (2018).

[54] M. Zhou, S. Yu, W. Yang, W.-k. Lou, F. Cheng, D. Zhang, and K. Chang, Current-induced spin polarization in monolayer InSe, Phys. Rev. B **100**, 245409 (2019).

[55] A. Ceferino, S. J. Magorrian, V. Zólyomi, D. A. Bandurin, A. K. Geim, A. Patanè, Z. D. Kovalyuk, Z. R. Kudrynskyi, I. V. Grigorieva, and I. V. Fal'ko, Tunable spin-orbit coupling in two-dimensional InSe, Phys. Rev. B **104**, 125432 (2021).

[56] G. W. Mudd, S. A. Svatek, T. Ren, A. Patanè, O. Makarovsky, L. Eaves, P. H. Beton, Z. D. Kovalyuk, G. V. Lashkarev, Z. R. Kudrynskyi *et al.*, Tuning the bandgap of exfoliated InSe nanosheets by quantum confinement, Adv. Mater. **25**, 5714 (2013).

[57] H. Cai, Y. Gu, Y.-C. Lin, Y. Yu, D. B. Geohegan, and K. Xiao, Synthesis and emerging properties of 2D layered III-VI metal chalcogenides, Appl. Phys. Rev. **6**, 041312 (2019).

[58] C. Zhang, B. Zheng, G. Wu, X. Liu, J. Wu, C. Yao, Y. Wang, Z. Tang, Y. Chen, L. Fang *et al.*, Controlled growth of vertically stacked In_2Se_3/WSe_2 heterostructures for ultrahigh responsivity photodetector, Nano Res. **17**, 1856 (2024).

[59] N. Balakrishnan, E. D. Steer, E. F. Smith, Z. R. Kudrynskyi, Z. D. Kovalyuk, L. Eaves, A. Patanè, and P. H. Beton, Epitaxial growth of γ-InSe and α, β, and γ-In_2Se_3 on ε-GaSe, 2D Mater. **5**, 035026 (2018).

[60] Y. Yan, S. Li, J. Du, H. Yang, X. Wang, X. Song, L. Li, X. Li, C. Xia, Y. Liu *et al.*, Reversible half wave rectifier based on 2D InSe/GeSe heterostructure with near-broken band alignment, Adv. Sci. **8**, 1903252 (2021).

[61] K. S. Novoselov, A. Mishchenko, A. Carvalho, and A. H. Castro Neto, 2D materials and van der Waals heterostructures, Science **353**, aac9439 (2016).

[62] T. Bjorkman, A. Gulans, A. V. Krasheninnikov, and R. M. Nieminen, van der Waals bonding in layered compounds from advanced density-functional first-principles calculations, Phys. Rev. Lett. **108**, 235502 (2012).

[63] C. Hua, F. Sheng, Q. Hu, Z.-A. Xu, Y. Lu, and Y. Zheng, Dialkali-metal monochalcogenide semiconductors with high mobility and tunable magnetism, J. Phys. Chem. Lett. **9**, 6695 (2018).

[64] C.-X. Xia, J. Du, X.-W. Huang, W.-B. Xiao, W.-Q. Xiong, T.-X. Wang, Z.-M. Wei, Y. Jia, J.-J. Shi, and J.-b. Li, Two-dimensional n-InSe/p-GeSe(SnS) van der Waals heterojunctions: High carrier mobility and broadband performance, Phys. Rev. B **97**, 115416 (2018).

[65] H. Bai, X. Wang, W. Wu, P. He, Z. a. Xu, S. A. Yang, and Y. Lu, Nonvolatile ferroelectric control of topological states in two-dimensional heterostructures, Phys. Rev. B **102**, 235403 (2020).

[66] S. Vajna, E. Simon, A. Szilva, K. Palotas, B. Ujfalussy, and L. Szunyogh, Higher-order contributions to the Rashba-Bychkov effect with application to the Bi/Ag(111) surface alloy, Phys. Rev. B **85**, 075404 (2012).

[67] Z. Y. Zhu, Y. C. Cheng, and U. Schwingenschlögl, Giant spin-orbit-induced spin splitting in two-dimensional transition-metal dichalcogenide semiconductors, Phys. Rev. B **84**, 153402 (2011).

[68] M. Zhou, D. Zhang, S. Yu, Z. Huang, Y. Chen, W. Yang, and K. Chang, Spin-charge conversion in InSe bilayers, Phys. Rev. B **99**, 155402 (2019).

[69] Y. Chen, Z. Tang, H. Shan, B. Jiang, Y. Ding, X. Luo, and Y. Zheng, Enhanced out-of-plane piezoelectric effect in In_2Se_3/transition metal dichalcogenide heterostructures, Phys. Rev. B **104**, 075449 (2021).

[70] A. David, P. Rakyta, A. Kormányos, and G. Burkard, Induced spin-orbit coupling in twisted graphene–transition metal dichalcogenide heterobilayers: Twistronics meets spintronics, Phys. Rev. B **100**, 085412 (2019).

[71] M. Milivojević, M. Gmitra, M. Kurpas, I. Štich, and J. Fabian, Proximity-enabled control of spin-orbit coupling in phosphorene symmetrically and asymmetrically encapsulated by WSe_2 monolayers, Phys. Rev. B **109**, 075305 (2024).

[72] A. Avsar, J. Y. Tan, T. Taychatanapat, J. Balakrishnan, G. K. W. Koon, Y. Yeo, J. Lahiri, A. Carvalho, A. S. Rodin, E. C. T. O'Farrell *et al.*, Spin-orbit proximity effect in graphene, Nat. Commun. **5**, 4875 (2014).